Research Article

Tunable N$_2$ Fixation Enabled by Ferroelectric Switching in Doped Graphene/In$_2$Se$_3$ Dual-Atom Catalysts

Mohammad Amin Akhound,* Maryam Soleimani, and Mahdi Pourfath*

Read Online

ACCESS | Metrics & More | Article Recommendations | Supporting Information

ABSTRACT: The electrochemical nitrogen reduction reaction (NRR) provides a sustainable alternative to ammonia synthesis. However, the development of catalysts with high activity and selectivity under ambient conditions remains a significant challenge. In this work, we propose a class of dual-atom catalysts (DACs), consisting of two metal atoms embedded in nitrogen-doped porous graphene (M$_2$NPG) supported on a ferroelectric α-In$_2$Se$_3$ monolayer. Using density functional theory (DFT) calculations, we explore the effect of ferroelectric polarization switching on the structural stability, catalytic performance, and reaction mechanisms of these DACs. By computationally screening 27 metal atoms as active sites, we identify four promising candidates (V, Co, Ru, and Ta) with V$_2$NPG@In$_2$Se$_3$ standing out due to its exceptional properties. The precise control of NRR pathways, along with tunable limiting potentials and selective product formation, can be achieved through the polarization switching of the α-In$_2$Se$_3$ monolayer. The combination of low limiting potential, abundant active sites, tunable catalytic behavior, and high selectivity against the hydrogen evolution reaction (HER) highlights the potential of V$_2$NPG@In$_2$Se$_3$ as a promising alternative to traditional single-atom catalysts. This work demonstrates a versatile strategy for integrating DACs with ferroelectric materials, offering valuable insights into designing next-generation catalysts for NRR and beyond.

KEYWORDS: nitrogen reduction reaction, dual-atom catalysts, ferroelectric materials, density functional theory, two-dimensional materials, α-In$_2$Se$_3$, electrocatalysis
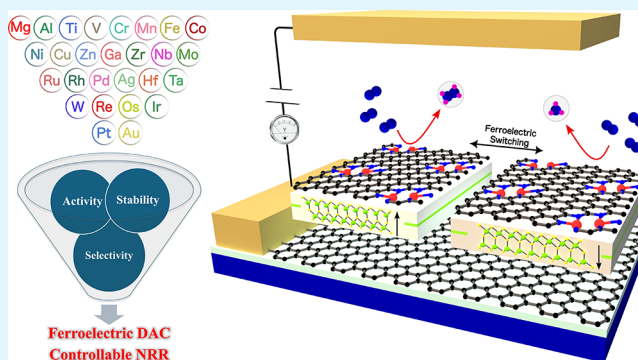
1. INTRODUCTION

The growing demand for sustainable energy solutions, driven by the rapid depletion of fossil fuel reserves, has accelerated the pursuit of green energy technologies. Among these, the electrochemical conversion of nitrogen (N$_2$) to ammonia (NH$_3$) is a sustainable alternative to the energy-intensive Haber-Bosch process.[1−5] However, efficient catalysts for the nitrogen reduction reaction (NRR) remain a challenge, especially for practical applications. The reaction kinetics are notably slow, and the process is highly competitive with the hydrogen evolution reaction (HER) in aqueous environments.[6,7] This competition severely limits the Faradaic efficiency (FE) of various catalysts, including metals,[8,9] metal oxides,[10,11] and transition metal chalcogenides,[12−14] resulting in FE values often well below optimal levels.

Single-atom catalysts (SACs), which consist of isolated metal atoms anchored on two-dimensional (2D) materials such as graphene or metal oxides, have shown great promise in addressing these challenges due to their high atom efficiency and precise control over catalytic processes.[15,16] These catalysts enhance the NRR by utilizing isolated single-atom active sites, where the electronic properties of the metal atoms are carefully tuned through their coordination environment. This enables effective nitrogen activation and supports ammonia synthesis.[17] Despite their advantages, SACs face challenges related to atom stability, as single metal atoms tend to aggregate under reactive conditions, diminishing their catalytic effectiveness. The performance of SACs is significantly influenced by the choice of the support material, which complicates their synthesis and limits their practical applications. Moreover, accurately characterizing single atoms remains a major challenge, further hindering their development for real-world applications.[18,19]
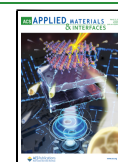
However, dual-atom catalysts (DACs) offer a promising solution by providing multiple active sites that can facilitate different reaction steps independently, optimizing each atom's role. This separation helps to overcome scaling relationships

that limit the activity of SACs, which struggle to balance the binding energies of the adsorbates. Therefore, DACs achieve improved activity and stability compared to SACs.[20] Recent studies have revealed that DACs can achieve significantly higher ammonia yield rates and FEs compared to SACs.[21−25]

Despite recent progress, there is still significant potential for developing novel catalysts with improved controllability, selectivity, and activity for large-scale industrial applications. 2D ferroelectric materials, such as α-In$_2$Se$_3$, have exhibited promising performance by switching polarization and modulating catalytic activity by adjusting electronic structure.[26,27] The unique characteristic of ferroelectric materials enables precise control over catalytic processes and enhances activity and selectivity compared with those of traditional catalysts. One study demonstrated that doping transition metal atoms onto ferroelectric α-In$_2$Se$_3$ monolayers (TM@In$_2$Se$_3$) can improve CO$_2$ reduction reactions by altering reaction pathways and final products through polarization switching.[28] The same ferroelectric switching effect has been observed for the electrocatalytic oxidation of CO on α-In$_2$Se$_3$ with selenium vacancy defects, doped with single metal atoms.[29] The study of ferroelectric heterostructures, such as Mo-BN@In$_2$Se$_3$ and WSe$_2$@In$_2$Se$_3$, exhibits either semiconducting or metallic properties based on polarization direction due to a built-in electric field and electron transfer, optimizing both photocatalytic and electrocatalytic reactions.[30] Furthermore, recent research indicates that heterostructures of graphene doped with single metal atoms on a ferroelectric layer, such as CoN$_3$ on α-In$_2$Se$_3$, show promising improvements in HERs due to polarization-induced electron redistribution and band state shifts, leading to better catalytic efficiency and stability.[31] These developments highlight the significant potential of 2D ferroelectric materials for the creation of next-generation controllable electrocatalysts.

While previous research on ferroelectric materials has focused solely on SACs, our study introduces a novel class of 2D heterostructures for NRR that integrate dual metal atoms with controllable ferroelectric properties. To achieve this, N-doped porous graphene containing metal dimers (M$_2$NPG) with excellent synthesizability[32−35] and superior NRR activity[36,37] is placed on top of the ferroelectric α-In$_2$Se$_3$ monolayer.[38,39] Through a systematic investigation of 27 metal atoms, we identify four metal atoms as highly stable active sites with promising catalytic performance. Among these, V$_2$NPG@In$_2$Se$_3$ demonstrates the ability to control reaction barriers, pathways, and final products of the NRR via polarization switching. The significance of this work lies in the achievement of a highly active, selective, and controllable catalyst that not only leverages the unique features of ferroelectric materials but also harnesses the advantages of DACs, including numerous active sites.

2. METHODS AND COMPUTATIONAL DETAILS

All calculations were performed using the spin-polarized density functional theory (DFT) methods, implemented through the Vienna Ab initio Simulation Package (VASP) software.[40,41] PBE-GGA spin-polarized approximation treats the exchange-correlation interactions, while the frozen-core projector augmented wave (PAW) approximation describes the interaction between ion and electron.[42−44] The Hubbard U parameter is not included in this study; however, a detailed analysis of the effect of the U parameter on the results can be found in the Supporting Information Section 1.[45−51] The long-range van der Waals (vdW) interactions between layers are described by the semiempirical DFT-D3 method in Grimme's scheme.[52] The NPG@α-

In$_2$Se$_3$ heterostructure is created by vertically stacking a $5 \times 5 \times 1$ NPG supercell[53] on a $3 \times 3 \times 1$ α-In$_2$Se$_3$ monolayer. The chosen supercell size for the NPG layer is well-established in the literature for DACs and ensures sufficient separation between periodic dual-atom sites, thereby minimizing artifacts arising from periodic boundary conditions.[54,55] To prepare the NPG layer, four carbon atoms were removed from the graphene center to create vacancies, which can accommodate the metal dimer. The six unsaturated carbon atoms surrounding the vacancies were replaced with nitrogen atoms to form the nitrogen-doped porous graphene structure.[34,35,56] The M$_2$NPG@α-In$_2$Se$_3$ heterostructure was then constructed by incorporating two metal atoms into the vacancy sites.

The lattice parameter of the NPG@α-In$_2$Se$_3$ heterostructure is 12.3 Å, which aligns well with previous studies.[31,57,58] The lattice mismatch in this structural model is 0.15%, which minimally impacts the computed total energies as well as the structural and electronic properties. A vacuum spacing of over 20 Å is introduced perpendicular to the surface to prevent interactions between periodic layers. The dipole correction is also applied to all asymmetric structures.[59] An energy cutoff of 500 eV is adopted for the plane-wave basis. In structural optimizations, the Brillouin zone is sampled with $5 \times 5 \times 1$ k-points using the γ-centered k-mesh, while the denser k-points of $10 \times 10 \times 1$ are used for electronic properties computations. The energy and force convergence thresholds for the self-consistent field (SCF) iteration are set to 10^{-5} eV and 0.01 eV/Å, respectively. The climbing image nudged elastic band (NEB) method[60] is employed to determine the transition state during the reactions.

Thermal stability was assessed through ab initio molecular dynamics (AIMD) simulations at room temperature (298.15 K), with the Nose-Hoover thermostat ensuring consistent temperature control.[61] The simulation ran for 5 ps with a time step of 1 fs, providing insights into the stability of the structure over time. In addition, the free energy diagram of the NRR is obtained using the computational hydrogen electrode (CHE) model proposed by Nørskov et al.[62] The free energy difference for each elemental reaction step is calculated as[63,64]

$$\Delta G = \Delta E + \Delta E_{ZPE} - T\Delta S \quad (1)$$

where ΔE represents the electronic energy difference obtained directly from DFT calculations, ΔE_{ZPE} denotes the change in zero-point energies, T is the temperature (set at 298.15 K), and ΔS is the entropy change. The effect of solvation on the free energy diagrams of the final candidates is further investigated in the Supporting Information Section 2.[65] Furthermore, grand canonical DFT calculations are performed, and the results are compared with constant-charge DFT calculations, which are further discussed in the Supporting Information Section 3.[66−68] The charge density difference (CDD) is calculated to evaluate the charge transfer between the surface and N$_2$ molecule using the following equation[69]:

$$\rho = \rho_{total} - \rho_{M_2NPG@In_2Se_3} - \rho_{N_2} \quad (2)$$

where ρ_{total}, $\rho_{M_2NPG@In_2Se_3}$, ρ_{N_2} are the charge of N$_2$ molecule adsorbed on the M$_2$NPG@In$_2$Se$_3$, free M$_2$NPG@In$_2$Se$_3$ and isolated N$_2$ molecule, respectively.

3. RESULTS AND DISCUSSION

3.1. Structural Models of Ferroelectric DACs. Different from ferroelectric SACs,[28,29,31] this study introduces a novel DAC where a 2D layer of M$_2$NPG is placed on top of a ferroelectric α-In$_2$Se$_3$ monolayer. Constructing a heterostructure rather than doping metal atoms directly on α-In$_2$Se$_3$ has several advantages. First, DACs cannot be achieved through direct doping; single-atom doping is typically limited to isolated metal atoms rather than pairs, which limits the catalytic versatility. Moreover, doping metal atoms into α-In$_2$Se$_3$ would likely face synthetic challenges, as creating homogeneously dispersed dopant sites on a layered ferro-
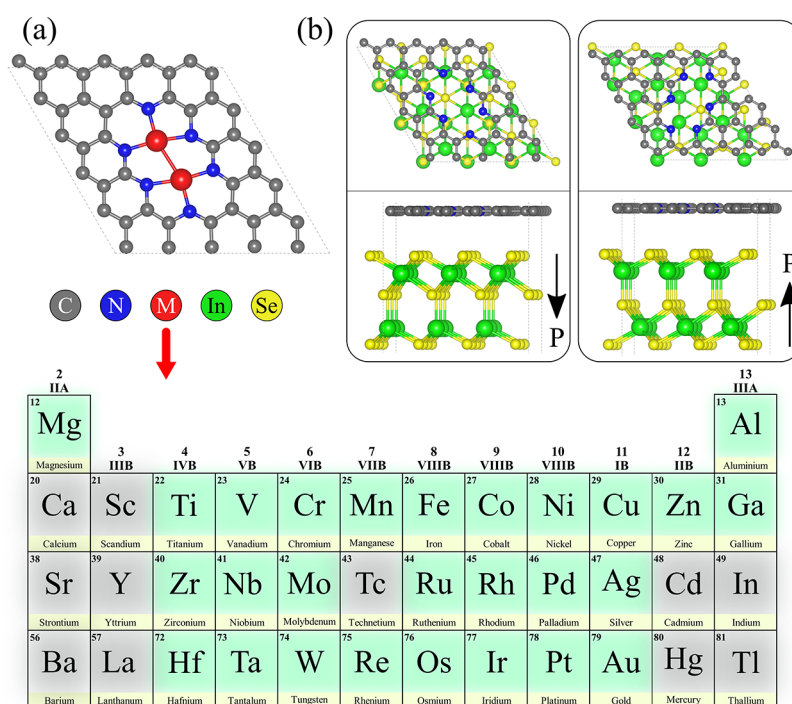
Figure 1. (a) Top view of the 2D M_2NPG monolayer, highlighting the various metal atoms considered in this study. (b) Top and side views of the optimized NPG@P↓In$_2$Se$_3$ and NPG@P↑In$_2$Se$_3$ heterostructures, with black arrows indicating the polarization direction of the α-In$_2$Se$_3$ monolayer.

electric substrate is complex and can lead to structural distortions or clustering, reducing catalytic efficiency and consistency.

In contrast, constructing a heterostructure with M_2NPG provides a more controllable platform for positioning dual metal atoms, facilitating easier synthesis and ensuring consistent active sites. Additionally, heterostructures inherently possess enhanced interfacial effects, allowing for fine-tuning of the catalytic properties through the interaction between NPG and the underlying polarized α-In$_2$Se$_3$. This layered approach leverages the intrinsic polarization of α-In$_2$Se$_3$ to modulate the electronic properties in M_2NPG, creating a flexible and effective DAC design for the NRR and overcoming limitations commonly faced in directly doped systems.[70]

The choice of α-In$_2$Se$_3$ as the bottom layer is based on its robust stability at room temperature and its experimentally demonstrated switchable polarization, providing a unique platform for designing controllable catalysts.[28,30,39,71] Furthermore, this material's versatility has also been highlighted in studies on tunable electronic and magnetoelectric devices, showcasing its potential for multifunctional applications.[58,72,73] This material consists of five covalently bonded monatomic layers arranged as Se−In−Se−In−Se, forming a triangular lattice.[38] The middle Se atoms are asymmetrically bonded to four neighboring In atoms, creating a noncentrosymmetric structure essential for ferroelectricity. The calculated lattice constant of monolayer α-In$_2$Se$_3$ is $a = 4.058$ Å, consistent with previous studies.[72−74] According to the electrostatic surface potential (ESP) of the α-In$_2$Se$_3$ monolayer, shown in Figure S1a, there is a significant asymmetry between the two surfaces of this material, with a potential difference of 1.23 eV. This disparity indicates the presence of an intrinsic electric field across the monolayer, which is proof of spontaneous polarization in ferroelectric materials. The electric dipole

moment is 0.095 eÅ per α-In$_2$Se$_3$ unit cell. The built-in electric field is highly advantageous for catalytic applications, as it can influence the adsorption and activation of reactant molecules by modifying the electronic environment at the catalyst surface.

Despite its advantageous ferroelectric properties, the sizable band gap of 1.46 eV in α-In$_2$Se$_3$ hinders its direct application in NRR.[75] Figure S2 illustrates that N_2 adsorption on both the P↑ and P↓ surfaces of the α-In$_2$Se$_3$ monolayer is weak, with minimal adsorption energy and a bond length of 1.113 Å, similar to the gas phase of the N_2 molecule. This physical adsorption behavior suggests that pristine α-In$_2$Se$_3$ alone is ineffective for activating N_2, as it lacks the ability to engage in the necessary electron transfer to weaken the N≡N bond. Typically, transition-metal atoms are introduced as catalytic sites due to their partially filled d orbitals, which can accept the electron density from N_2 and back-donate to its antibonding orbitals, effectively facilitating bond weakening. Although main-group metal elements are rarely explored as catalytic active sites, modulating the s/p-band filling of these metals can also lead to enhanced catalytic activity.[76] Therefore, we introduced a dual-atom-metal-doped nitrogen porous graphene (M_2NPG) layer atop α-In$_2$Se$_3$ to leverage these mechanisms. M_2NPG offers a high density of active sites with tunable metal d orbitals, enabling strong hybridization with nitrogen molecular orbitals and promoting electron transfer to destabilize the N≡N bond. Furthermore, this configuration has been successfully synthesized with various metals and is recognized for its robust catalytic performance in NRR.[32−37]

Based on the distinct polarization directions of the α-In$_2$Se$_3$ monolayer surfaces, we identified two heterostructures with ferroelectric polarization oriented either upward (P↑) or downward (P↓), as shown in Figure 1b. The lattice parameters of the α-In$_2$Se$_3$ monolayer and the NPG layer were carefully
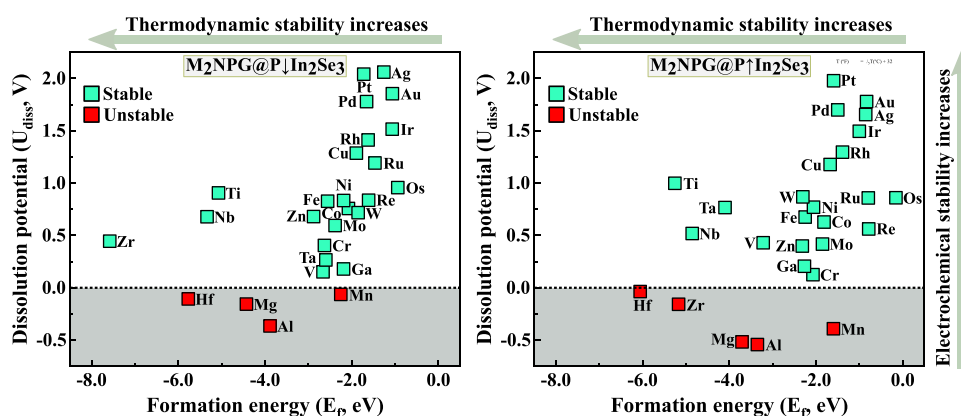
Figure 2. Computed formation energies and dissolution potentials of metal atoms in the $M_2NPG@P{\downarrow}In_2Se_3$ and $M_2NPG@P{\uparrow}In_2Se_3$ heterostructures.

selected to ensure minimal strain, maintaining a near-perfect match with only 0.48% of strain applied equally to both layers. This careful selection preserves the structural integrity of the heterostructure and avoids distortions that could impact the electronic and catalytic properties. To further refine the structural model, the interlayer distance between the NPG layer and the α-In$_2$Se$_3$ monolayer was systematically varied (2.5 3.0, and 3.5 Å) during the initial setup. After structural optimization, the interlayer distances in the NPG@P{\downarrow}In$_2$Se$_3$ and NPG@P{\uparrow}In$_2$Se$_3$ configurations converged to 3.45 and 3.44 Å, respectively, in agreement with previously reported values.[57,58] The ESP of these heterostructures, shown in Figure S1b,c, indicates that the direction of polarization influences the electric field within the NPG layer. The magnitudes of the electric dipoles are 1.05 and 0.47 eÅ for the two oppositely polarized systems, respectively. Consequently, this effect alters the electronic states at the interface, allowing for tunable electronic properties that respond to polarization switching.

The projected density of states (PDOS) for the NPG layer on the P{\uparrow} and P{\downarrow} surfaces of α-In$_2$Se$_3$ is shown in Figure S3, alongside the PDOS of pristine α-In$_2$Se$_3$ for reference. Pristine α-In$_2$Se$_3$ has a wide indirect band gap, measured at 1.46 eV with HSE06 and 0.78 eV with GGA-PBE, showing a clear distinction between In and Se states near the Fermi level, which highlights its semiconducting nature. Interfacing α-In$_2$Se$_3$ with NPG modifies its electronic structure, inducing metallic properties. This metallic behavior improves the carrier mobility, making it highly beneficial for electrocatalytic reactions. In the P{\downarrow} configuration, significant hybridization between the carbon atoms in NPG and the In and Se atoms near the Fermi level is observed. This hybridization, which enhances charge transfer at the interface, suggests that P{\downarrow} polarization promotes a more conductive environment in the NPG layer. In the P{\uparrow} configuration, however, the PDOS reveals reduced hybridization and fewer states near the Fermi level, implying weaker interaction and lower charge transfer compared to the P{\downarrow} case.

To enable efficient catalysis, we incorporated two metal atoms into the vacancy sites within the NPG layer, creating a series of homonuclear DACs, as illustrated in Figure 1a. In principle, all 3d, 4d, and 5d transition metals, as well as main group metals, can serve as metal centers in M$_2$NPG. However, due to their toxic or radioactive properties, certain metals were excluded from consideration in this study. We focused on 27 metal atoms, including 24 transition metals (excluding Sc, Y,

La, Tc, Cd, and Hg) and 3 main group metals (Mg, Al, and Ga) as central atoms in the 2D M$_2$NPG layer. To eliminate potential artifacts arising from stacking order variations, the selected vacancy sites and metal incorporation strategy were designed to ensure symmetry. The vacancy sites were large enough and symmetrically aligned above the α-In$_2$Se$_3$ monolayer to create a uniform interface. This symmetry ensures that all possible atomic arrangements in the underlying layer are equally accessible to the metal atoms in the NPG layer (top view of Figure 1b). As a result, any rotation or shift of the metal atoms or vacancy sites does not alter the electronic interactions or the catalytic properties. In the following sections, we outline the screening methods used to identify stable ferroelectric DACs and investigate their potential catalytic activity for the NRR.

3.2. Stability Screening. Using the abovementioned criteria, 54 heterostructures of M$_2$NPG@P{\downarrow}In$_2$Se$_3$ and M$_2$NPG@P{\uparrow}In$_2$Se$_3$ were generated and optimized, as illustrated in Figures S4 and S5, respectively. Table S1 summarizes the structural parameters of these heterostructures. The thermodynamic and electrochemical stabilities of these structures were subsequently evaluated by calculating the formation energy E_f, binding energy E_b, and dissolution potential U_{diss}, defined as follows[77,78]:

$$E_f = (E_{M_2NPG@In_2Se_3} - E_{NPG@In_2Se_3} - 2E_M)/2 \tag{3}$$

$$E_b = (E_{M_2NPG@In_2Se_3} - E_{NPG@In_2Se_3} - 2\mu_M)/2 \tag{4}$$

$$U_{diss} = U_{diss}^\circ(\text{metal, bulk}) - E_f/ne \tag{5}$$

Here, E_M and μ_M represent the total energies of a single metal atom from its most stable bulk phase and an isolated metal atom, respectively. $E_{M_2NPG@In_2Se_3}$ and $E_{NPG@In_2Se_3}$ denote the total energies of the substrate with and without metal atoms. $U_{diss}^\circ(\text{metal, bulk})$ is the standard dissolution potential of the bulk metal, and n is the number of electrons involved in dissolution. According to these definitions, systems with negative E_f and E_b are considered thermodynamically stable, indicating that metal atoms prefer to disperse into the vacancy defects of the graphene layer rather than forming metal clusters.[78] Furthermore, for a structure to be electrochemically stable, the U_{diss} vs SHE should be positive.[22] The exact values of E_f, E_b, and U_{diss} can be found in Table S2.

As shown in Figure 2, all of the investigated metal dimers are thermodynamically stable within the graphene layer, as
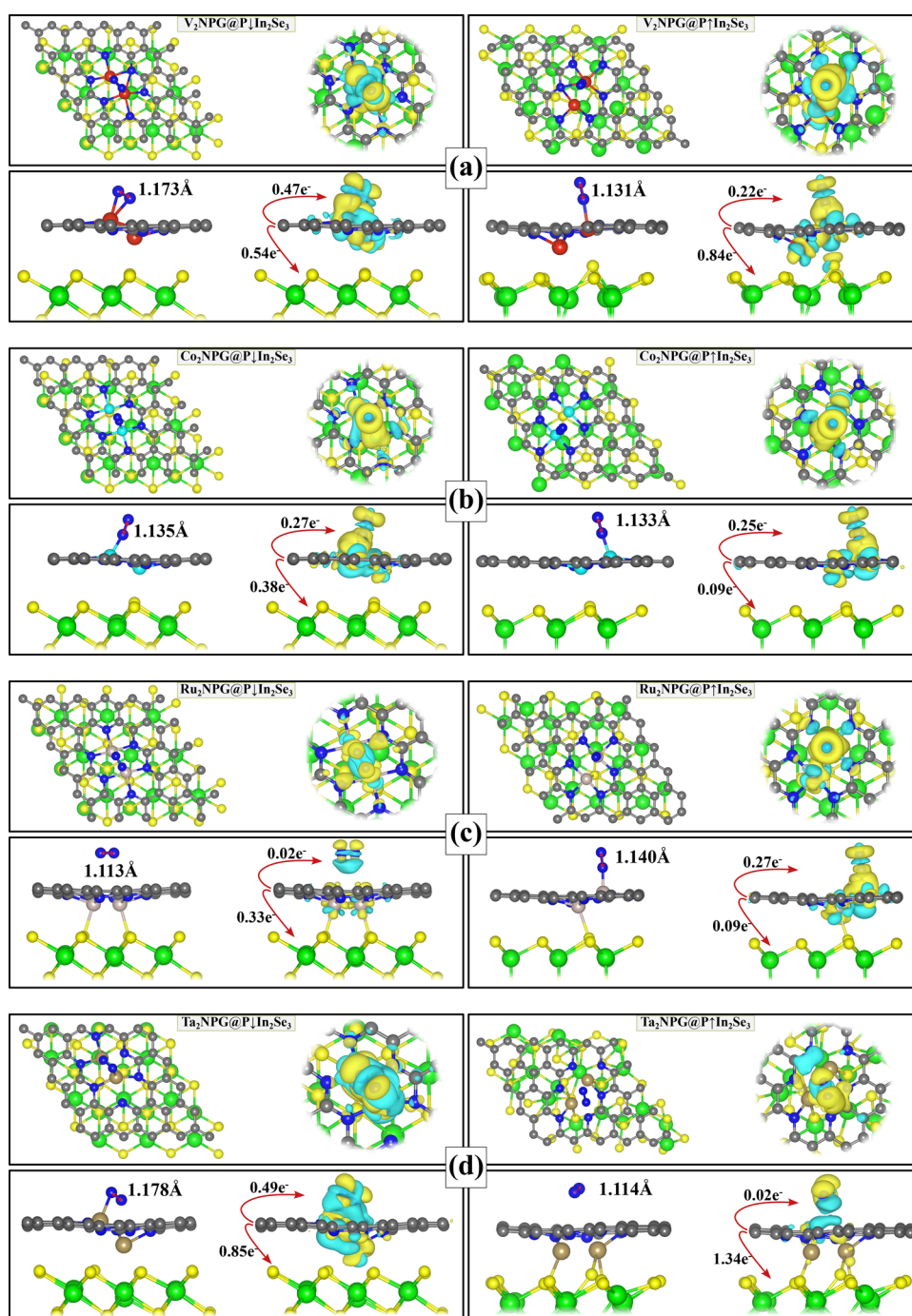
Figure 3. Top and side views of the optimized adsorption configurations and charge density differences of N_2 molecule on $M_2NPG@P{\downarrow}In_2Se_3$ and $M_2NPG@P{\uparrow}In_2Se_3$ heterostructures with (a) V_2, (b) Co_2, (c) Ru_2, and (d) Ta_2 as active sites. The charge depletion and accumulation were depicted by cyan and yellow, respectively. To enhance visualization, different isosurface values are used for the P↓ and P↑ structures, which are (a) 0.0015 and 0.0008 $e/Å^3$, (b) 0.0013 and 0.0013↓$e/Å^3$, (c) 0.0001 and 0.0014 $e/Å^3$, and (d) 0.0011 and 0.0001 $e/Å^3$, respectively.

indicated by their calculated E_f values well below zero. However, five metal atoms exhibit negative U_{diss} values in at least one of the P↑ or P↓ configurations. Since the aim is to control the catalytic reaction by switching polarization directions, it is crucial that the structures remain stable in both orientations. Consequently, ten structures containing Mn, Hf, Zr, Mg, and Al metals embedded in the graphene layer are excluded due to their electrochemical instability in an acidic environment.

3.3. N_2 Adsorption. The first step in the electrochemical conversion of N_2 to NH_3 is the adsorption and activation of the N_2 molecule. Generally, all stable heterostructures can serve as suitable substrates for the activation of N_2. To explore the adsorption behavior of N_2 on the remaining stable heterostructures, three distinct configurations were considered: bridge adsorption, adsorption on top of the first metal atom, and adsorption on top of the second metal atom. The configuration with the lowest adsorption energy was selected as the most favorable site for further analysis. The adsorption

energies of N_2 on 22 metal atoms, for both the P↓ and P↑ surfaces, are provided in Table S3. As shown in this table, 18 metals exhibited either desorption or physical adsorption with adsorption energies greater than −0.25 eV for both the P↓ and P↑ orientations. However, four metal atoms (V, Co, Ru, and Ta) adsorbed N_2 chemically with notable adsorption energies in at least one orientation. Interestingly, these structures demonstrated distinct adsorption behaviors that were controlled by the ferroelectric polarization of the α-In$_2$Se$_3$ monolayer. The detailed adsorption properties of the N_2 molecule on these heterostructures are summarized in Figure 3 and Table 1.

Table 1. Adsorption Energies ($\Delta H_{ads}^{N_2^*}$) and Adsorption Configurations ($N_2^{conf.}$) of the N_2 Molecule on M_2NPG@In$_2$Se$_3$ Heterostructures^a

catalyst	$\Delta H_{ads}^{N_2^*}$ (eV)	$N_2^{conf.}$	$\Delta H_{ads}^{H^*}$ (eV)	ΔG^{H^*} (eV)
V$_2$NPG@P↓In$_2$Se$_3$	−0.69	Side-on	−0.10	0.16
V$_2$NPG@P↑In$_2$Se$_3$	−0.51	End-on	−0.03	0.26
Co$_2$NPG@P↓In$_2$Se$_3$	−0.57	End-on	−0.20	0.17
Co$_2$NPG@P↑In$_2$Se$_3$	−0.52	End-on	−0.53	−0.21
Ru$_2$NPG@P↓In$_2$Se$_3$	−0.18	Physisorption	−0.26	0.02
Ru$_2$NPG@P↑In$_2$Se$_3$	−0.61	End-on	−0.37	−0.12
Ta$_2$NPG@P↓In$_2$Se$_3$	−0.99	Side-on	−1.12	−0.88
Ta$_2$NPG@P↑In$_2$Se$_3$	−0.17	Physisorption	−0.14	0.16

^{a}Hydrogen adsorption energies ($\Delta H_{ads}^{H^*}$) and Gibbs free energies (ΔG^{H^*}) are also included for selectivity comparison.

The activation of N_2 on M_2NPG@In$_2$Se$_3$ surfaces is crucial for the NRR, facilitating electron transfer that weakens the N≡N bond and promotes robust adsorption. This interaction involves both σ and π bonds: the unoccupied d orbitals of the metal dimers accept electrons from the σ and π orbitals of N_2, forming bonding states that stabilize the adsorbed N_2 molecule. Simultaneously, the occupied d orbitals of the metal back-donate electrons into N_2's antibonding π^* orbitals, weakening the triple bond by populating these antibonding states. Charge density analysis reveals significant electron transfer to the adsorbed N_2 molecule for V$_2$NPG@P↓In$_2$Se$_3$ and Ta$_2$NPG@P↓In$_2$Se$_3$, with values of 0.47 and 0.49 e charge transfer, respectively, indicating strong side-on N_2 adsorption configurations.

Polarization switching in M_2NPG@In$_2$Se$_3$ induces significant changes in the PDOS of metal d orbitals, leading to noticeable shifts in the d-band center (ϵ_d), as shown in Figure S6. According to the d-band center model, the position of ϵ_d relative to the Fermi level governs the interaction strength between metal surfaces and adsorbates, influencing both the adsorption energy and catalytic activity. A higher ϵ_d generally correlates with stronger adsorption, as the antibonding states shift higher in energy, reducing their occupation and thus increasing the binding strength. Conversely, a lower ϵ_d weakens adsorption by filling antibonding states, leading to a reduced interaction with the adsorbate.

The impact of polarization on ϵ_d directly influences N_2 activation and its subsequent hydrogenation pathways. As shown in Figure 4, for V$_2$NPG@In$_2$Se$_3$, the ϵ_d values shift from 0.25 eV (P↑) to 0.09 eV (P↓), aligning with an increase in adsorption strength from −0.51 to −0.69 eV. This downward

shift in ϵ_d reduces the occupancy of antibonding states, thereby strengthening the V−N_2 interaction and promoting activation. A similar trend is observed in Co$_2$NPG@In$_2$Se$_3$, where a lower ϵ_d in the P↓ state (−1.33 eV) compared to P↑ (−1.19 eV) results in stronger N_2 adsorption (−0.57 eV vs −0.52 eV). However, Ru$_2$NPG@In$_2$Se$_3$ exhibits different behavior. Despite a downward shift in ϵ_d (−1.86 eV for P↓), the adsorption energy weakens (−0.18 eV), suggesting that the d-band center has shifted too low, filling antibonding states and thereby weakening the interaction. This deviation from the expected trend highlights the complexity of the d-band interactions, especially for elements with more delocalized d-states.

Among the studied materials, Ta$_2$NPG@In$_2$Se$_3$ demonstrated the most pronounced polarization-dependent adsorption behavior. In the P↑ state, the relatively high ϵ_d of 0.21 eV results in weak N_2 adsorption (−0.17 eV). However, upon switching to P↓, ϵ_d decreases significantly to −0.19 eV, strengthening the adsorption dramatically to −0.99 eV. This substantial shift underscores the critical role of polarization control in tuning the adsorption energetics. Notably, in the pristine state, Ta$_2$NPG@In$_2$Se$_3$ exhibits ϵ_d values of 0.19 eV (P↑) and −0.06 eV (P↓), reinforcing its strong polarization-dependent behavior. These results demonstrate that polarization switching effectively modulates ϵ_d, allowing precise control over the adsorption strength and catalytic performance. The findings further highlight the importance of tuning electronic states through external electric fields to enhance catalytic activity, particularly for systems with strong polarization effects.

To quantitatively capture N_2 interaction with M_2NPG@In$_2$Se$_3$, crystal orbital Hamilton population (COHP) analysis[79] was performed, and the results are presented in Figure 4. In COHP, negative values indicate bonding interactions, while positive values reflect antibonding contributions. The integrated COHP (ICOHP), calculated by summing contributions from all occupied states up to the Fermi level, provides a net measure of the bonding or antibonding interactions between the metal dimers and N_2. A more negative ICOHP value reflects a stronger interaction, indicating greater back-donation into the π^* orbitals of N≡N. This weakens the N≡N bond, facilitating its activation. Bonding states shifting to higher energies (rightward) suggest weakened bonding due to reduced orbital occupancy, while antibonding states shifting to lower energies (leftward) indicate enhanced metal back-donation, further promoting N_2 activation.

The differences in ICOHP values between structures reveal the effects of adsorption modes and polarization. For example, V$_2$NPG@P↓In$_2$Se$_3$ adopts a side-on configuration with an ICOHP of −0.59, while V$_2$NPG@P↑In$_2$Se$_3$ favors an end-on configuration with an ICOHP of −0.41. Similarly, Co$_2$NPG@P↓In$_2$Se$_3$ and Co$_2$NPG@P↑In$_2$Se$_3$ exhibit end-on adsorption, showing substantial charge transfer and moderately negative ICOHP values (−0.47 and −0.41), indicating effective d−π^* interactions and strong N_2 activation. In contrast, Ru$_2$NPG@P↓In$_2$Se$_3$ and Ta$_2$NPG@P↑In$_2$Se$_3$ have negligible ICOHP values (−0.02 and −0.01), suggesting weak physisorption of N_2. However, reversing the polarization significantly increases the ICOHP values (−0.63 and −0.69), signifying full N_2 activation and making it ready for hydrogenation. Notably, side-on adsorption configurations generally yield more negative ICOHP values and stronger adsorption energies
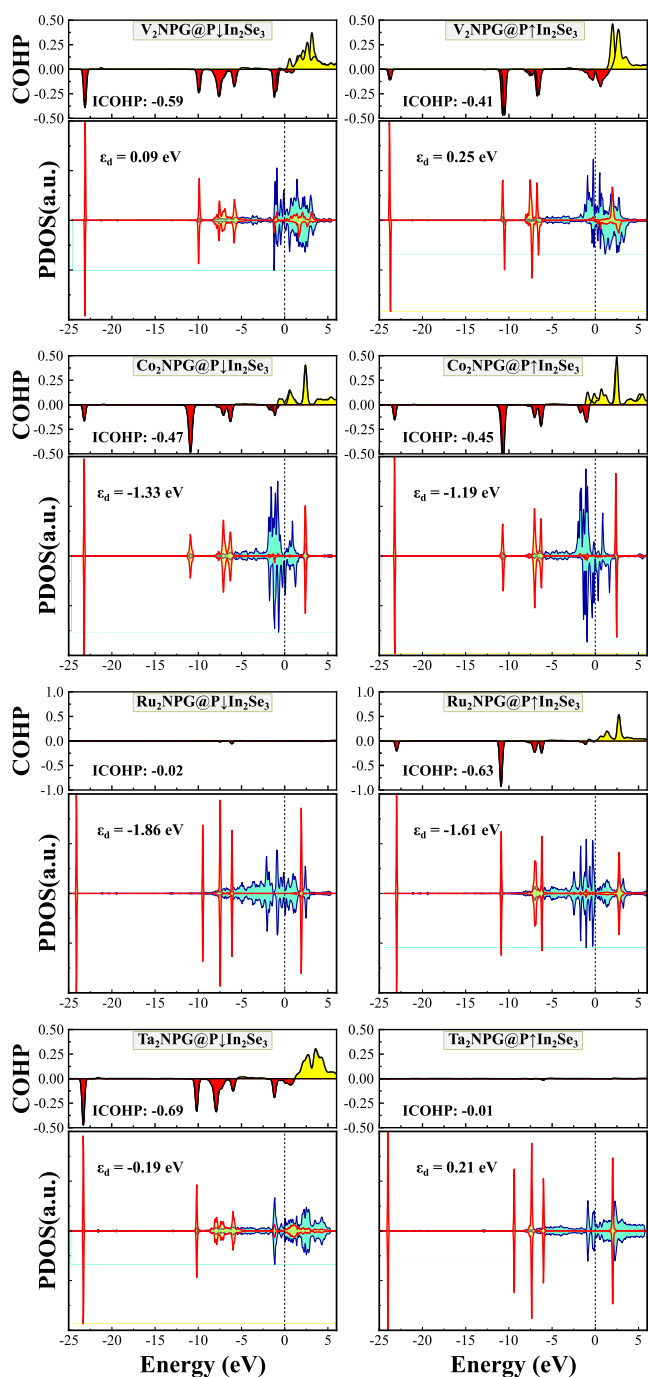
Figure 4. PDOS of N$_2$ molecule adsorbed on M$_2$NPG@In$_2$Se$_3$ (M = V, Co, Ru, and Ta) systems with the P↑ and P↓ polarization directions of α-In$_2$Se$_3$. The blue and red lines correspond to the d orbitals of the metal atoms and the p orbitals of the N$_2$ molecule, respectively. The ϵ_d values denote the d-band center of metal atoms relative to the Fermi level, averaged over both the spin-up and spin-down states. Additionally, the COHP of N$_2$ on each structure are calculated, with bonding and antibonding states represented by red and yellow, respectively.
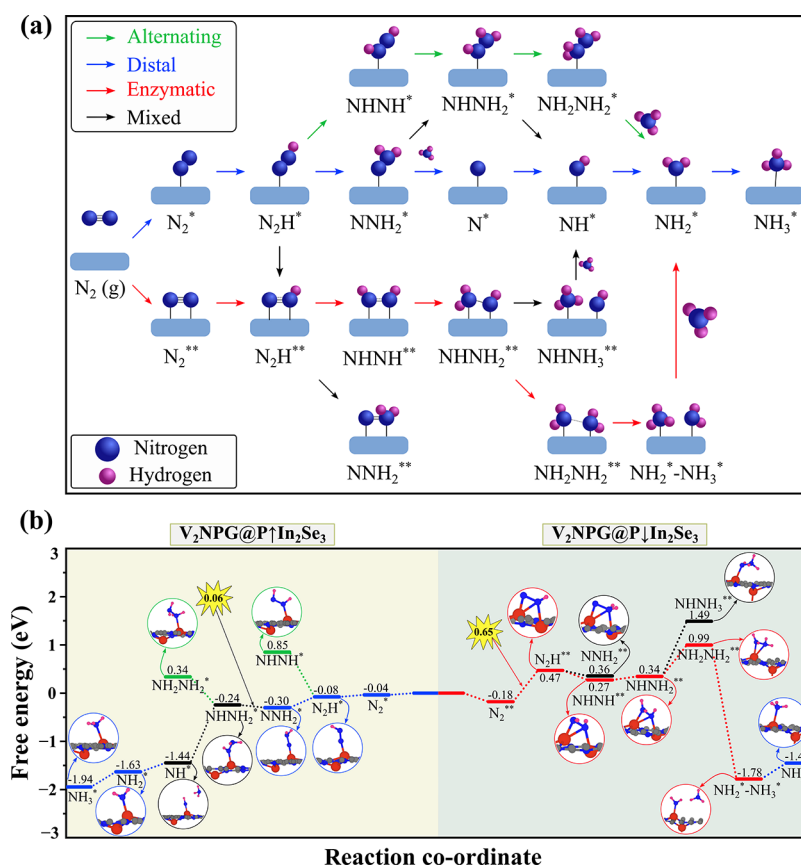
V$_2$NPG layer to P↓In$_2$Se$_3$. This transfer partially compensates for the polarization, reducing the built-in electric field within the heterostructure. In this configuration, the potential difference across the heterostructure surfaces is 0.08 eV, with a built-in electric field of 8.31×10^7 V/m (dipole moment = 0.061 eÅ). Conversely, when the V$_2$NPG layer is placed on top of P↑In$_2$Se$_3$, atomic and electronic reconstructions occur, leading to an increased electron transfer of 0.84 e to P↑In$_2$Se$_3$ to counteract the depolarizing field induced by polarization charges. This significantly raises the potential difference to 2.15 eV and the built-in electric field to 2.07×10^9 V/m (dipole moment = 1.56 eÅ). These reconstructions influence N$_2$ adsorption by modifying the binding energies and the availability of adsorption sites. Notably, the strength of the built-in electric field can be estimated by $E = P/\epsilon Sd$, where P is the intrinsic dipole moment, ϵ is the dielectric constant, S is the surface area, and d is the thickness of the heterostructure.

The adsorption of hydrogen (H*), a crucial competing side reaction in the NRR process, not only consumes protons and electrons but also obstructs active sites, as noted in reference.[80] Figure S7 presents the optimized adsorption configurations of H* on M$_2$NPG@P↓In$_2$Se$_3$ and M$_2$NPG@P↑In$_2$Se$_3$ heterostructures, showcasing their interaction with active sites. To evaluate the selectivity of catalysts for the HER and NRR, the free energy difference of H* (ΔG^{H*}) was used as a selectivity descriptor, with the results summarized in Table 1. For V$_2$NPG@P↓In$_2$Se$_3$ and V$_2$NPG@P↑In$_2$Se$_3$, the ΔG^{H*} were calculated as 0.16 and 0.26 eV, respectively, indicating that HER is less likely to occur on these surfaces compared to other materials, such as Co$_2$NPG@P↑In$_2$Se$_3$, Ru$_2$NPG@P↑In$_2$Se$_3$, and Ta$_2$NPG@P↓In$_2$Se$_3$. In the latter materials, the spontaneous HER in one polarization direction increases their susceptibility to H* poisoning on the surface. This strong affinity for H* adsorption reduces their selectivity and limits effective polarization control under reaction conditions, emphasizing the superior selectivity of V$_2$NPG@In$_2$Se$_3$.

3.4. Catalytic Activity. To explore the catalytic activity and NRR mechanism, V$_2$NPG@P↓In$_2$Se$_3$ and V$_2$NPG@P↑In$_2$Se$_3$ were selected due to their promising selectivity and controlled hydrogen adsorption behavior. These materials provide an ideal platform for investigating how the polarization direction influences reaction dynamics and how the ferroelectric surface modulates the empty and occupied d orbitals, thereby affecting the NRR process.

In the industrial Haber–Bosch process, the ammonia synthesis follows a dissociative mechanism, where the N≡N bond is first cleaved, generating isolated nitrogen atoms that subsequently undergo hydrogenation to form NH$_3$. This process requires extreme conditions due to the high energy needed to break the strong triple bond of N$_2$. In contrast, electrocatalytic NRR typically proceeds via associative pathways, which can be classified into four main types: distal,[81] alternating,[82] enzymatic,[83] and mixed pathways.[84] These pathways differ in how nitrogen atoms interact with protons and electrons on the catalyst surface, influencing the selectivity and efficiency.

As illustrated in Figure 5a, in the distal pathway, the hydrogenation predominantly occurs at the terminal nitrogen atom, while the surface-bound N atom remains unreacted until the first NH$_3$ molecule is released. This stepwise process ensures exclusive NH$_3$ production with no byproducts. The alternating pathway, however, involves the simultaneous

compared to end-on configurations, implying better catalytic performance for NRR in side-on adsorption modes.

To further investigate the differences in N$_2$ adsorption, we examined the dipole properties of the V$_2$NPG layer. The results indicate that when the V$_2$NPG layer is placed on top of P↓In$_2$Se$_3$, an electron transfer of 0.54 e occurs from the

Figure 5. (a) Schematic illustration of potential reaction mechanisms during the NRR process. (b) Gibbs free energy diagrams of the NRR on $V_2NPG@P\uparrow In_2Se_3$ and $V_2NPG@P\downarrow In_2Se_3$ heterostructures.

hydrogenation of both nitrogen atoms, potentially leading to the formation of intermediates such as N_2H_4. While industrial N_2H_4 production typically relies on the oxidative coupling of NH_3 in the Haber−Bosch process, direct catalytic approaches for synthesizing N_2H_4 from N_2 have received limited attention,[85,86] despite significant advancements in NH_3 synthesis catalysts. The enzymatic pathway follows a distinct side-on binding configuration, where both nitrogen atoms attach to the catalyst surface, allowing for sequential hydrogenation. This orientation offers a unique reaction mechanism, further broadening the possible routes for the electrocatalytic NRR.

Figure 5b (left) presents the free energy profile and optimized geometries for the elementary steps in the distal pathway. Initially, N_2 adsorbs onto the $V_2NPG@P\uparrow In_2Se_3$ cluster in an end-on configuration, where it undergoes hydrogenation through proton adsorption and electron transfer, forming the N_2H^* intermediate. In this step, the proton attaches to the distal nitrogen atom, resulting in an elongated N−N bond length of 1.213 Å compared to the preadsorbed N_2 molecule (1.131 Å). This first step is slightly exergonic with a ΔG of −0.04 eV. In the second step, another proton and electron are sequentially added to the N_2H^* species, producing the NNH_2^* intermediate. This step further elongates the N−N bond to 1.314 Å. The reaction is energetically favorable, with a ΔG of −0.22 eV. In contrast, the alternating pathway for forming $NHNH^*$ from N_2H^* is unfavorable, requiring a high ΔG of +0.93 eV, indicating a kinetically challenging step.

In the third step, the $NHNH_2^*$ intermediate is formed via mixed pathways. This step is associated with a small uphill ΔG value of 0.06 eV, with further elongation of the N−N bond to 1.412 Å. The alternating pathway involving the formation of $NH_2NH_2^*$ from $NHNH_2^*$ is also energetically unfavorable under the current conditions. The fourth step involves the release of the first NH_3 molecule. Successive proton-coupled electron transfers occur at the NH_2 site of $NHNH_2^*$, leading to a significant downhill ΔG of −1.20 eV. Following this, an NH species remains bound to the V atom with a V−NH bond length of 1.664 Å. In the fifth step, the reduction of NH^* to NH_2^* occurs with a ΔG of −0.19 eV, elongating the V−NH_2 bond to 1.879 Å. In the final step, NH_2^* reacts with an additional proton and electron to form NH_3^*, with a ΔG of −0.31 eV, and the V−NH_3 bond length of 2.155 Å. Overall, the distal pathway is characterized by the protonation of NNH_2^* to form $NHNH_2^*$ as the potential rate-limiting step, given its slightly positive ΔG of 0.06 eV among all elementary steps.

After evaluating the catalytic performance of the $V_2NPG@P\uparrow In_2Se_3$ system, we now focus on the opposite polarization direction ($V_2NPG@P\downarrow In_2Se_3$) to assess its influence on N_2 activation and hydrogenation. Figure 5b (right) presents the Gibbs free energy profile along with the optimized structures of the elementary steps in the enzymatic pathway, which progresses through six sequential steps. In the first step, the side-on configuration of N_2 on the $V_2NPG@P\downarrow In_2Se_3$ cluster undergoes hydrogenation through proton adsorption coupled with electron transfer, forming the N_2H^* species. This step is associated with an uphill ΔG of 0.65 eV, with the bond length
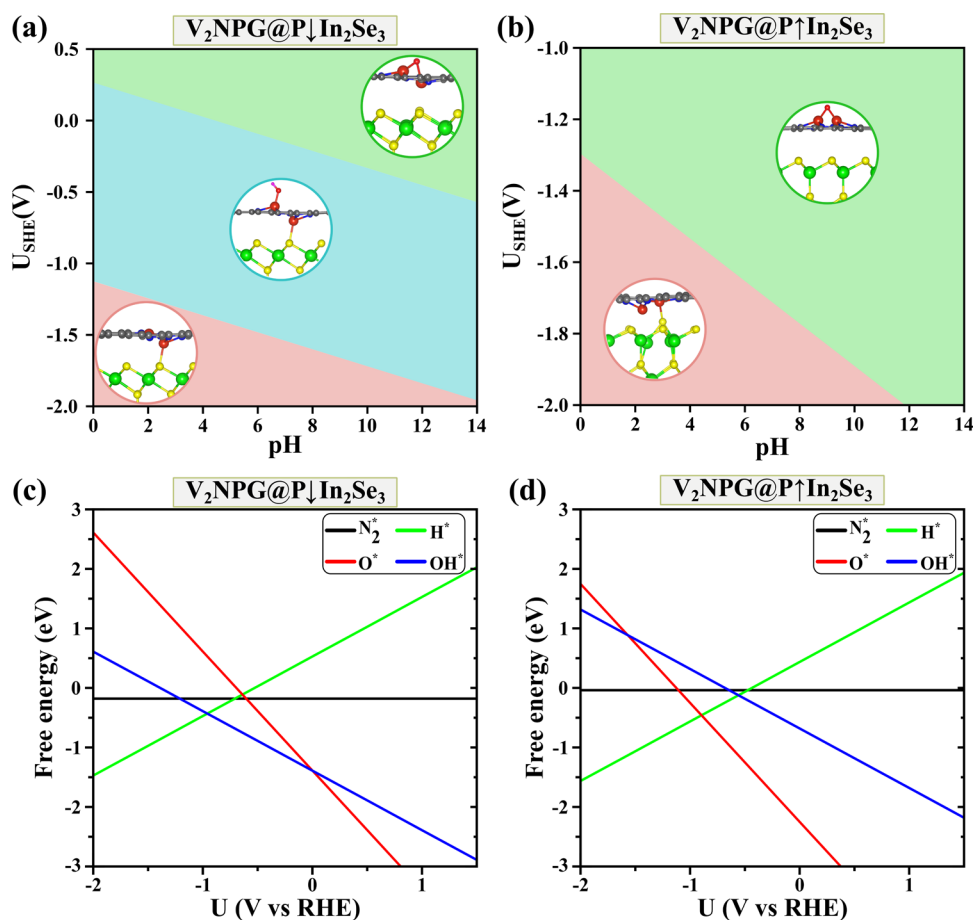
Figure 6. (a) Surface Pourbaix diagrams of $V_2NPG@P{\downarrow}In_2Se_3$ and (b) $V_2NPG@P{\uparrow}In_2Se_3$. (c) Competitive adsorption of N_2^*, H^*, OH^*, and O^* on $V_2NPG@P{\downarrow}In_2Se_3$ and (d) $V_2NPG@P{\uparrow}In_2Se_3$ as a function of the electrode potential.

of N−N in the N_2H^* species being 1.363 Å, compared to the preadsorbed N_2 molecule (1.173 Å). In the second step, the N_2H^* species is further hydrogenated to form NHNH*, accompanied by a favorable downhill ΔG of 0.20 eV. Additionally, NNH_2 can form with another downhill ΔG of 0.11 eV. The third step involves the hydrogenation of NHNH* to $NHNH_2^*$, which requires overcoming a small ΔG of 0.07 eV. In the fourth step, the $NHNH_2^*$ species undergoes further hydrogenation to form $NH_2NH_2^*$. This transformation demands an ΔG of 0.65 eV, which is higher than the corresponding step in the distal pathway, where ΔG is only 0.06 eV. The fifth step sees the release of the first NH_3 molecule, with the N−N bond lengths increasing progressively throughout the intermediate stages (1.413 Å for NHNH*, 1.430 Å for $NHNH_2^*$, and 1.452 Å for $NH_2NH_2^*$). This highly favorable step has a downhill ΔG of −2.77 eV. The reaction leaves an NH_2 group bound to the catalyst surface, with a V−NH_2^* bond length of 1.866 Å. Finally, in the sixth step, the NH_2^* species is hydrogenated to produce the second NH_3 molecule. This step is endergonic with a ΔG of 0.33 eV, and the V−NH_3 bond length in this step is 2.151 Å.

Furthermore, the kinetics of proton transfer in the potential-limiting steps, specifically $NNH_2^* \rightarrow NHNH_2^*$ on $V_2NPG@P{\uparrow}In_2Se_3$ and $N_2^* \rightarrow N_2H^*$ on $V_2NPG@P{\downarrow}In_2Se_3$, were analyzed using the Zundel $H_5O_2^+$ complex as the solvated proton donor (Figure S11). Initially, the shortest distance between the H

atom from $H_5O_2^+$ and the N atom at the active site was set to 3.0 Å, which decreased to 2.0 and 1.9 Å in the transition state for $V_2NPG@P{\uparrow}In_2Se_3$ and $V_2NPG@P{\downarrow}In_2Se_3$, respectively. The calculated activation barriers for these steps are 0.10 and 0.36 eV, suggesting that proton transfer is kinetically feasible under ambient conditions and could be further enhanced at more negative applied voltages.

The N_2 reduction mechanism on the $V_2NPG@In_2Se_3$ catalyst, including the reaction barriers for each step and the limiting potentials, is strongly dependent on polarization. While NH_3 is the primary product in the main pathways, switching the polarization can partially or even completely alter the N_2 reduction pathway, potentially leading to the formation of different final products. Specifically, switching from the $NHNH_2$ pathway on $V_2NPG@P{\downarrow}In_2Se_3$ changes the reaction process from an enzymatic to a distal-mixed mechanism. Interestingly, although N_2H_4 cannot be directly formed on the $V_2NPG@P{\downarrow}In_2Se_3$ catalyst, polarization reversal reactivates the catalytic reduction on the $V_2NPG@P{\uparrow}In_2Se_3$ surface. Under these conditions, the N_2H_4 molecule can transition from a side-on to an end-on configuration as a byproduct under reasonable limiting potentials. This polarization-dependent switching offers significant potential for fine-tuning the selectivity of N_2 reduction reactions, enabling the controlled production of both NH_3 and N_2H_4 by modulating the polarization direction of the catalyst.
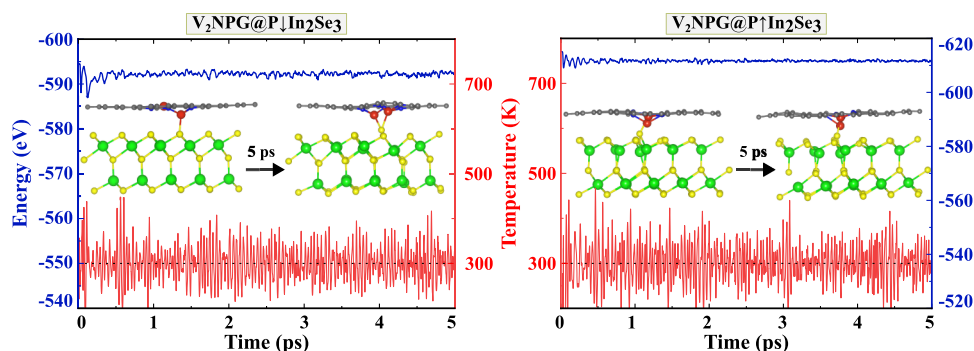
Figure 7. Fluctuations in the total potential energy (blue line) and temperature (red line) during the AIMD simulations of the V$_2$NPG@P↑In$_2$Se$_3$ and V$_2$NPG@P↓In$_2$Se$_3$ heterostructures. The insets display side views of the structures at both the beginning and end of the simulations.

The NRR selectivity and performance of V$_2$NPG@In$_2$Se$_3$ were evaluated by analyzing the adsorption behavior of key adsorbates (N$_2^*$, H*, OH*, and O*) as a function of the applied electrode potential. The equilibrium reaction can be represented as

V$_2$NPG@In$_2$Se$_3$ + xH$_2$O ⇌ V$_2$NPG@In$_2$Se$_3$@O$_x^*$H$_y^*$ + (2x − y) + (H$^+$ + e$^-$) where V$_2$NPG@In$_2$Se$_3$@O$_x^*$H$_y^*$ denotes the catalyst surface covered by OH*, and O* species.[87] Notably, a detailed analysis revealed distinct adsorption behaviors for the two polarization states of α-In$_2$Se$_3$. For the P↓In$_2$Se$_3$ configuration, the low limiting potential of −0.65 V falls within the potential window where OH adsorption is predominant, while both H and O adsorption are effectively suppressed (Figure 6a,c). This ensures that under operating conditions, the catalyst surface remains largely available for N$_2$ adsorption, thereby enhancing the NRR selectivity. In contrast, for P↑In$_2$Se$_3$, the limiting potential of −0.06 V indicates that O and OH are in competition with N$_2$ adsorption, while H adsorption remains suppressed (Figure 6b,d). This suggests that while some oxygen-containing intermediates (OH* and O*) may compete with N$_2$ adsorption, the catalyst still retains a significant capacity for selective nitrogen activation. Tuning the applied potential and optimizing the catalytic environment are essential to achieve selective adsorption of N$_2^*$ over O* and OH*. Importantly, the results highlight that H adsorption is strongly influenced by the applied potential within the limiting potential range, reinforcing that V$_2$NPG@In$_2$Se$_3$ can effectively mitigate the HER while maintaining an active surface for N$_2$ activation.

For controllable catalysis to be successful, it is crucial that both the ferroelectric and catalysts themselves maintain good stability. To evaluate the stability of V$_2$NPG@In$_2$Se$_3$, AIMD simulations were conducted at room temperature, as shown in Figure 7. The results indicate that although α-In$_2$Se$_3$ tends to attract the V atoms of the NPG layer, resulting in a slight reduction in the distance between the two V atoms due to their interaction with α-In$_2$Se$_3$, the NPG layer preserves its structural integrity, preventing the detachment of the V atoms and their adsorption onto the α-In$_2$Se$_3$. Atomic fluctuations, resulting from thermal disturbances and the interaction between α-In$_2$Se$_3$ and the V atoms, are observed in the V$_2$NPG@P↓In$_2$Se$_3$ structure compared to the initial configuration, while the V$_2$NPG@P↑In$_2$Se$_3$ structure remains largely unchanged, retaining its original form. Overall, both structures demonstrate stability over 5 ps, with no metal clustering, phase transitions, or significant energy changes detected.

A schematic device design is presented for N$_2$ reduction using doped graphene/α-In$_2$Se$_3$ DACs, as shown in Figure 8.
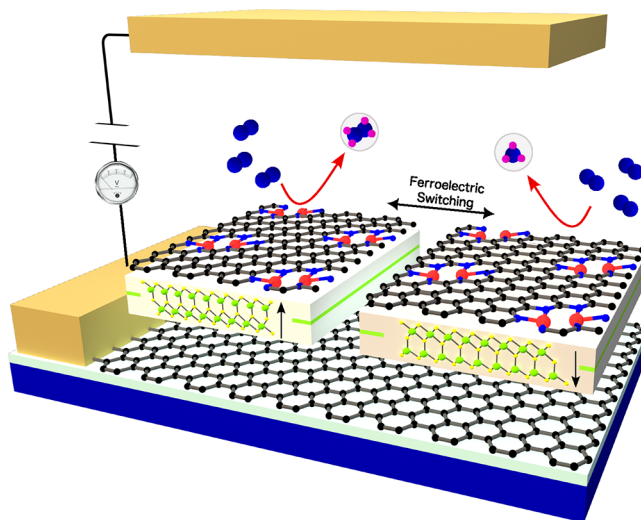
Figure 8. Schematic representation of a ferroelectric-controlled NRR facilitated by the DAC of V$_2$NPG@In$_2$Se$_3$. The heterostructure, comprising V$_2$NPG deposited on an α-In$_2$Se$_3$ monolayer, is placed between two electrodes. By reversal of the bias voltage, the polarization direction of the α-In$_2$Se$_3$ monolayer can be switched, enabling precise modulation of the catalytic NRR process.

Drawing inspiration from the recently fabricated and predicted ferroelectric diodes based on 2D α-In$_2$Se$_3$ layers,[28,88] this design harnesses the unique polarization-dependent catalytic properties of the system. By reversal of the bias direction, ferroelectric switching provides precise control over the reaction pathways and products. Notably, the existence of P↑ and P↓ polarization states in α-In$_2$Se$_3$ has been experimentally demonstrated, further supporting the feasibility of such devices.[39,71,88] Furthermore, a comparison of the proposed catalysts with previously reported ones,[22,89−93] as presented in Table S4, reveals that while V$_2$NPG@P↓In$_2$Se$_3$ exhibits a limiting potential comparable to existing catalysts, V$_2$NPG@P↑In$_2$Se$_3$ achieves a remarkably low limiting potential of −0.06 eV. This exceptionally low limiting potential, combined with the polarization-switchable nature of the proposed catalyst, highlights a unique advantage of this work and underscores its potential significance in the field.

4. CONCLUSIONS

In conclusion, based on DFT calculations, we investigated the feasibility of polarization-controlled NRR using DACs based on $M_2NPG@In_2Se_3$ heterostructures. Out of the 27 metals screened, four were identified as highly active for N_2 activation, with $V_2NPG@In_2Se_3$ emerging as the most promising candidate. Detailed analysis of its performance revealed a low limiting potential of −0.06 and −0.65 V on P↑In_2Se_3 and P↓In_2Se_3, respectively, along with tunable reaction pathways and product selectivity enabled by ferroelectric polarization switching. The DAC design enhances the density of active sites and offers controllable catalytic behavior, distinguishing it from traditional SACs. This work highlights the transformative role of ferroelectric materials in catalyst design, paving the way for next-generation, tunable electrocatalysts for NRR and other catalytic reactions. The integration of DACs with switchable ferroelectric materials introduces a paradigm shift toward highly selective and adaptable catalytic systems for diverse applications.

■ ASSOCIATED CONTENT

ⓈⒾ Supporting Information

The Supporting Information is available free of charge at https://pubs.acs.org/doi/10.1021/acsami.4c21092.

> Information about the PBE + U, grand canonical DFT, and the climbing image nudged elastic band (NEB) calculations, the effect of solvation on the free energy diagrams, the electrostatic surface potential (ESP), projected density of states (PDOS) of the α-In_2Se_3 monolayer and $NPG@In_2Se_3$ heterostructures, along with all optimized configurations of $M_2NPG@In_2Se_3$ heterostructures, their structural parameters, cohesive energies, formation energies, dissolution potentials, binding energies, and hydrogen adsorption configurations for both P↑ and P↓ polarization directions of α-In_2Se_3 monolayer and comparison of the proposed catalysts from this work with reported ones from the literature (PDF)

■ AUTHOR INFORMATION

Corresponding Authors

Mohammad Amin Akhound − *School of Electrical and Computer Engineering, College of Engineering, University of Tehran, Tehran 14395-515, Iran; CAMD, Department of Physics, Technical University of Denmark, DK - 2800 Kongens Lyngby, Denmark;* ⓞ orcid.org/0009-0009-1670-4591; Email: aminakhound@ut.ac.ir, akhound@dtu.dk

Mahdi Pourfath − *School of Electrical and Computer Engineering, College of Engineering, University of Tehran, Tehran 14395-515, Iran; Institute for Microelectronics/ E360, TU Wien, A-1040 Vienna, Austria;* ⓞ orcid.org/ 0000-0002-8053-578X; Email: pourfath@ut.ac.ir, pourfath@iue.tuwien.ac.at

Author

Maryam Soleimani − *Dipartimento di Scienza dei Materiali, Università di Milano − Bicocca, 20125 Milano, Italy*

Complete contact information is available at:
https://pubs.acs.org/10.1021/acsami.4c21092

Notes

The authors declare no competing financial interest.

■ ACKNOWLEDGMENTS

■ REFERENCES

(1) Sarangi, P. K.; Srivastava, R. K.; Gitanjali, J.; Sathiyan, G.; Venkatesan, G.; Kandasamy, S. Exploring cutting-edge advances in green ammonia production and storage technologies. *Fuel* **2024**, *371*, No. 131863.

(2) Smith, C.; Hill, A. K.; Torrente-Murciano, L. Current and future role of Haber−Bosch ammonia in a carbon-free energy landscape. *Energy Environ. Sci.* **2020**, *13*, 331−344.

(3) Chen, J. G.; Crooks, R. M.; Seefeldt, L. C.; Bren, K. L.; Bullock, R. M.; Darensbourg, M. Y.; Holland, P. L.; Hoffman, B.; Janik, M. J.; Jones, A. K.; Kanatzidis, M. G.; King, P.; Lancaster, K. M.; Lymar, S. V.; Pfromm, P.; Schneider, W. F.; Schrock, R. R.; et al. Beyond fossil fuel−driven nitrogen transformations. *Science* **2018**, *360*, No. eaar6611.

(4) Shi, L.; Yin, Y.; Wang, S.; Sun, H. Rational Catalyst Design for N2Reduction under Ambient Conditions: Strategies toward Enhanced Conversion Efficiency. *ACS Catal.* **2020**, *10*, 6870−6899.

(5) Foster, S. L.; Bakovic, S. I.; Duda, R. D.; Maheshwari, S.; Milton, R. D.; Minteer, S. D.; Janik, M. J.; Renner, J. N.; Greenlee, L. F. Catalysts for nitrogen reduction to ammonia. *Nature Catalysis* **2018**, *1*, 490−500.

(6) Singh, A. R.; Rohr, B. A.; Schwalbe, J. A.; Cargnello, M.; Chan, K.; Jaramillo, T. F.; Chorkendorff, I.; Nørskov, J. K. Electrochemical Ammonia Synthesis—The Selectivity Challenge. *ACS Catal.* **2017**, *7*, 706−709.

(7) Niu, L.; An, L.; Wang, X.; Sun, Z. Effect on electrochemical reduction of nitrogen to ammonia under ambient conditions: Challenges and opportunities for chemical fuels. *Journal of Energy Chemistry* **2021**, *61*, 304−318.

(8) Krebsz, M.; Hodgetts, R. Y.; Johnston, S.; Nguyen, C. K.; Hora, Y.; MacFarlane, D. R.; Simonov, A. N. Reduction of dinitrogen to ammonium through a magnesium-based electrochemical process at close-to-ambient temperature. *Energy Environ. Sci.* **2024**, *17*, 4481−4487.

(9) Yang, Y.; Zhao, S.; Pang, Y.; Tang, G.; Song, Y.; Jiang, M.; Li, C.-P. Promoting electrochemical nitrogen fixation by nanoporous AuCu alloys. *Chem. Commun.* **2023**, *59*, 12132−12135.

(10) Han, X.; Zhou, W.; Huang, X.; Yu, H.; Yang, F.; Chen, S.; Wang, J. Enhancing electrocatalytic N2 reduction to NH3 by introducing Ni heteroatoms into NiCuOx electrocatalyst. *Catalysis Science & Technology* **2024**, *14*, 3691−3698.

(11) Yang, M.-L.; Jin, Z.-X.; Cao, X.-X.; Wang, X.-M.; Ma, H.-Y.; Pang, H.-J.; Yang, G.-X. Polyoxometalates-derived ternary metal oxides electrocatalyst for N2 reduction under ambient conditions. *Tungsten* **2024**, *6*, 428−437.

(12) Fei, H.; Guo, T.; Xin, Y.; Wang, L.; Liu, R.; Wang, D.; Liu, F.; Wu, Z. Sulfur vacancy engineering of MoS2 via phosphorus incorporation for improved electrocatalytic N2 reduction to NH3. *Applied Catalysis B: Environmental* **2022**, *300*, No. 120733.

(13) Yang, M.; Jin, Z.; Wang, C.; Cao, X.; Wang, X.; Ma, H.; Pang, H.; Tan, L.; Yang, G. Fe Foam-Supported FeS2−MoS2 Electrocatalyst for N2 Reduction under Ambient Conditions. *ACS Appl. Mater. Interfaces* **2021**, *13*, 55040−55050.

(14) Chen, S.; Fang, D.; Zhou, Z.; Zhao, Z.; Yang, Y.; Dai, Z.; Shi, J. B-doped MoS2/MoO2 heterostructure catalyst for the electrocatalytic reduction of N2 to NH3. *Catal. Lett.* **2024**, *154*, 4055−4064.

(15) Xu, H.; Cheng, D.; Cao, D.; Zeng, X. C. RETRACTED ARTICLE: A universal principle for a rational design of single-atom electrocatalysts. *Nature Catalysis* **2018**, *1*, 339−348.

(16) Hussain, M. I.; Farooq, M. U.; Xia, M.; Ren, X.; Zairov, R. R.; Harb, M. Single-atom catalysts for electrocatalytic applications: Synthetic strategies, in-situ characterization, and future challenges. *Applied Materials Today* **2024**, *36*, No. 102037.

(17) Choi, C.; Back, S.; Kim, N. Y.; Lim, J.; Kim, Y. H.; Jung, Y. Suppression of Hydrogen Evolution Reaction in Electrochemical N2 Reduction Using Single-Atom Catalysts: A Computational Guideline. *ACS Catal.* 2018, *8*, 7517−7525.

(18) Li, J.; Chen, C.; Xu, L.; Zhang, Y.; Wei, W.; Zhao, E.; Wu, Y.; Chen, C. Challenges and Perspectives of Single-Atom-Based Catalysts for Electrochemical Reactions. *JACS Au* 2023, *3*, 736−755.

(19) Cheng, N.; Zhang, L.; Doyle-Davis, K.; Sun, X. Single-Atom Catalysts: From Design to Application. *Electrochemical Energy Reviews* 2019, *2*, 539−573.

(20) Li, L.; Yuan, K.; Chen, Y. Breaking the Scaling Relationship Limit: From Single-Atom to Dual-Atom Catalysts. *Accounts of Materials Research* 2022, *3*, 584−596.

(21) Liang, M.; Shao, X.; Lee, H. Recent Developments of Dual Single-Atom Catalysts for Nitrogen Reduction Reaction. *Chem.−Eur. J.* 2024, *30*, No. e202302843.

(22) Guo, X.; Gu, J.; Lin, S.; Zhang, S.; Chen, Z.; Huang, S. Tackling the Activity and Selectivity Challenges of Electrocatalysts toward the Nitrogen Reduction Reaction via Atomically Dispersed Biatom Catalysts. *J. Am. Chem. Soc.* 2020, *142*, 5709−5721.

(23) Liu, Y.; Zhang, H.; Cheng, X. Unveiling the Mechanism of Nitrogen Fixation by Single-Atom Catalysts and Dual-Atom Catalysts Anchored on Defective Boron Nitride Nanotubes. *Energy Fuels* 2023, *37*, 13271−13281.

(24) Zhang, Z.; Huang, X.; Xu, H. Anchoring an Fe Dimer on Nitrogen-Doped Graphene toward Highly Efficient Electrocatalytic Ammonia Synthesis. *ACS Appl. Mater. Interfaces* 2021, *13*, 43632−43640.

(25) Lv, X.; Wei, W.; Huang, B.; Dai, Y.; Frauenheim, T. High-throughput screening of synergistic transition metal dual-atom catalysts for efficient nitrogen fixation. *Nano Lett.* 2021, *21*, 1871−1878.

(26) Wei, X.; Domingo, N.; Sun, Y.; Balke, N.; Dunin-Borkowski, R. E.; Mayer, J. Progress on emerging ferroelectric materials for energy harvesting, storage and conversion. *Adv. Energy Mater.* 2022, *12*, No. 2201199.

(27) Kim, H. S. Computational design of a switchable hetero-structure electrocatalyst based on a two-dimensional ferroelectric In2Se3material for the hydrogen evolution reaction. *Journal of Materials Chemistry A* 2021, *9*, 11553−11562.

(28) Ju, L.; Tan, X.; Mao, X.; Gu, Y.; Smith, S.; Du, A.; Chen, Z.; Chen, C.; Kou, L. Controllable CO2 electrocatalytic reduction via ferroelectric switching on single atom anchored In2Se3 monolayer. *Nat. Commun.* 2021, *12*, 5128.

(29) Zhou, Z.; Hu, T.; Kan, E. Tunable Single-Atom Catalysis of CO Oxidation on a Transition Metal-Anchored Defective In2Se3Monolayer. *J. Phys. Chem. C* 2023, *127*, 12548−12557.

(30) Ju, L.; Ma, Y.; Tan, X.; Kou, L. Controllable Electrocatalytic to Photocatalytic Conversion in Ferroelectric Heterostructures. *J. Am. Chem. Soc.* 2023, *145*, 26393−26402.

(31) Wan, T. L.; Liu, J.; Tan, X.; Liao, T.; Gu, Y.; Du, A.; Smith, S.; Kou, L. Rational design of 2D ferroelectric heterogeneous catalysts for controllable hydrogen evolution reaction. *Journal of Materials Chemistry A* 2022, *10*, 22228−22235.

(32) Wang, J.; Huang, Z.; Liu, W.; Chang, C.; Tang, H.; Li, Z.; Chen, W.; Jia, C.; Yao, T.; Wei, S.; Wu, Y.; Li, Y. Design of N-Coordinated Dual-Metal Sites: A Stable and Active Pt-Free Catalyst for Acidic Oxygen Reduction Reaction. *J. Am. Chem. Soc.* 2017, *139*, 17281−17284.

(33) Wang, J.; et al. Synergistic effect of well-defined dual sites boosting the oxygen reduction reaction. *Energy Environ. Sci.* 2018, *11*, 3375−3379.

(34) Han, X.; Ling, X.; Yu, D.; Xie, D.; Li, L.; Peng, S.; Zhong, C.; Zhao, N.; Deng, Y.; Hu, W. Atomically dispersed binary Co-Ni sites in nitrogen-doped hollow carbon nanocubes for reversible oxygen reduction and evolution. *Adv. Mater.* 2019, *31*, No. 1905622.

(35) Ye, W.; Chen, S.; Lin, Y.; Yang, L.; Chen, S.; Zheng, X.; Qi, Z.; Wang, C.; Long, R.; Chen, M.; Zhu, J.; Gao, P.; Song, L.; Jiang, J.; Xiong, Y. Precisely Tuning the Number of Fe Atoms in Clusters on

(36) Ma, D.; Wang, Y.; Liu, L.; Jia, Y. Electrocatalytic nitrogen reduction on the transition-metal dimer anchored N-doped graphene: performance prediction and synergetic effect. *Phys. Chem. Chem. Phys.* 2021, *23*, 4018−4029.

(37) Liu, Y.; Song, B.; Huang, C.-X.; Yang, L.-M. Dual transition metal atoms embedded in N-doped graphene for electrochemical nitrogen fixation under ambient conditions. *Journal of Materials Chemistry A* 2022, *10*, 13527−13543.

(38) Ding, W.; Zhu, J.; Wang, Z.; Gao, Y.; Xiao, D.; Gu, Y.; Zhang, Z.; Zhu, W. Prediction of intrinsic two-dimensional ferroelectrics in In2Se3 and other III2-VI3 van der Waals materials. *Nat. Commun.* 2017, *8*, No. 14956.

(39) Xue, F.; Hu, W.; Lee, K.; Lu, L.; Zhang, J.; Tang, H.; Han, A.; Hsu, W.; Tu, S.; Chang, W.; Lien, C.; He, J.; Zhang, Z.; Li, L.; Zhang, X.; et al. Room-temperature ferroelectricity in hexagonally layered α-In2Se3 nanoflakes down to the monolayer limit. *Adv. Funct. Mater.* 2018, *28*, No. 1803738.

(40) Kohn, W.; Sham, L. J. Self-Consistent Equations Including Exchange and Correlation Effects. *Phys. Rev.* 1965, *140*, A1133−A1138.

(41) Kresse, G.; Furthmüller, J. Efficient iterative schemes for ab initio total-energy calculations using a plane-wave basis set. *Phys. Rev. B* 1996, *54*, 11169−11186.

(42) Blöchl, P. E. Projector augmented-wave method. *Phys. Rev. B* 1994, *50*, 17953−17979.

(43) Kresse, G.; Joubert, D. From ultrasoft pseudopotentials to the projector augmented-wave method. *Phys. Rev. B* 1999, *59*, 1758−1775.

(44) Perdew, J. P.; Burke, K.; Ernzerhof, M. Generalized Gradient Approximation Made Simple. *Phys. Rev. Lett.* 1996, *77*, 3865−3868.

(45) Huang, M.; Fabris, S. CO adsorption and oxidation on ceria surfaces from DFT+ U calculations. *J. Phys. Chem. C* 2008, *112*, 8643−8648.

(46) Tolba, S. A.; Gameel, K. M.; Ali, B. A.; Almossalami, H. A.; Allam, N. K.; Yang, G.; Tolba, S. A.The DFT+U: Approaches, accuracy, and applications. *Density Functional Calculations-Recent Progresses of Theory and Application*; IntechOpen, 2018, *1*, 5772.

(47) Hu, Z.; Metiu, H. Choice of U for DFT+ U calculations for titanium oxides. *J. Phys. Chem. C* 2011, *115*, 5841−5845.

(48) Bhola, K.; Varghese, J. J.; Dapeng, L.; Liu, Y.; Mushrif, S. H. Influence of Hubbard U parameter in simulating adsorption and reactivity on CuO: Combined theoretical and experimental study. *J. Phys. Chem. C* 2017, *121*, 21343−21353.

(49) Fronzi, M.; Piccinin, S.; Delley, B.; Traversa, E.; Stampfl, C. Water adsorption on the stoichiometric and reduced CeO 2 (111) surface: A first-principles investigation. *Phys. Chem. Chem. Phys.* 2009, *11*, 9188−9199.

(50) Zhang, Z.; Xiao, J.; Chen, X.-J.; Yu, S.; Yu, L.; Si, R.; Wang, Y.; Wang, S.; Meng, X.; Wang, Y.; et al. Reaction mechanisms of well-defined metal−N4 sites in electrocatalytic CO2 reduction. *Angew. Chem., Int. Ed.* 2018, *57*, 16339−16342.

(51) Stahl, B.; Bredow, T. Critical assessment of the DFT+ U approach for the prediction of vanadium dioxide properties. *J. Comput. Chem.* 2020, *41*, 258−265.

(52) Grimme, S. Semiempirical GGA-type density functional constructed with a long-range dispersion correction. *J. Comput. Chem.* 2006, *27*, 1787−1799.

(53) Li, H.; Zhao, Z.; Cai, Q.; Yin, L.; Zhao, J. Nitrogen electroreduction performance of transition metal dimers embedded into N-doped graphene: a theoretical prediction. *Journal of Materials Chemistry A* 2020, *8*, 4533−4543.

(54) Zhao, W.; Zhang, L.; Luo, Q.; Hu, Z.; Zhang, W.; Smith, S.; Yang, J. Single Mo1 (Cr1) atom on nitrogen-doped graphene enables highly selective electroreduction of nitrogen into ammonia. *ACS Catal.* 2019, *9*, 3419−3425.

(55) Jia, S.; Zhu, H.; Cao, R.; Wu, Q.; Wu, C.; Zhou, Q.; Liu, P.; Li, B.; Li, A.; Li, Y. Efficient nitrogen-doped graphene supported

heteronuclear diatomic electrocatalyst for nitrogen reduction reaction: D-band center assisted rapid screening. *Int. J. Hydrogen Energy* **2024**, *83*, 367−377.

(56) Luo, M.; Liu, C.; Peera, S. G.; Liang, T. Atomic level N-coordinated Fe dual-metal embedded in graphene: an efficient double atoms catalyst for CO oxidation. *Colloids Surf., A* **2021**, *621*, No. 126575.

(57) Wan, T. L.; Shang, J.; Gu, Y.; Kou, L. Ferroelectric controlled gas adsorption in doped graphene/In2Se3 heterostructure. *Adv. Mater. Technol.* **2022**, *7*, No. 2100463.

(58) Shang, J.; Tang, X.; Gu, Y.; Krasheninnikov, A. V.; Picozzi, S.; Chen, C.; Kou, L. Robust magnetoelectric effect in the decorated graphene/In2Se3heterostructure. *ACS Appl. Mater. Interfaces* **2021**, *13*, 3033−3039.

(59) Neugebauer, J.; Scheffler, M. Adsorbate-substrate and adsorbate-adsorbate interactions of Na and K adlayers on Al(111). *Phys. Rev. B* **1992**, *46*, 16067−16080.

(60) Henkelman, G.; Uberuaga, B. P.; Jónsson, H. A climbing image nudged elastic band method for finding saddle points and minimum energy paths. *J. Chem. Phys.* **2000**, *113*, 9901−9904.

(61) Nosé, S. A unified formulation of the constant temperature molecular dynamics methods. *J. Chem. Phys.* **1984**, *81*, 511−519.

(62) Nørskov, J. K.; Rossmeisl, J.; Logadottir, A.; Lindqvist, L.; Kitchin, J. R.; Bligaard, T.; Jónsson, H. Origin of the Overpotential for Oxygen Reduction at a Fuel-Cell Cathode. *J. Phys. Chem. B* **2004**, *108*, 17886−17892.

(63) Nørskov, J. K.; Rossmeisl, J.; Logadottir, A.; Lindqvist, L.; Kitchin, J. R.; Bligaard, T.; Jonsson, H. Origin of the overpotential for oxygen reduction at a fuel-cell cathode. *J. Phys. Chem. B* **2004**, *108*, 17886−17892.

(64) Montoya, J. H.; Tsai, C.; Vojvodic, A.; Nørskov, J. K. The challenge of electrochemical ammonia synthesis: a new perspective on the role of nitrogen scaling relations. *ChemSusChem* **2015**, *8*, 2180−2186.

(65) Mathew, K.; Sundararaman, R.; Letchworth-Weaver, K.; Arias, T.; Hennig, R. G. Implicit solvation model for density-functional study of nanocrystal surfaces and reaction pathways. *J. Chem. Phys.* **2014**, *140*, No. 084106.

(66) Islam, S.; Khezeli, F.; Ringe, S.; Plaisance, C. An implicit electrolyte model for plane wave density functional theory exhibiting nonlinear response and a nonlocal cavity definition. *J. Chem. Phys.* **2023**, *159*, 234117.

(67) Tezak, C. R.; Singstock, N. R.; Alherz, A. W.; Vigil-Fowler, D.; Sutton, C. A.; Sundararaman, R.; Musgrave, C. B. Revised Nitrogen Reduction Scaling Relations from Potential-Dependent Modeling of Chemical and Electrochemical Steps. *ACS Catal.* **2023**, *13*, 12894−12903.

(68) Pedersen, P. D.; Melander, M. M.; Bligaard, T.; Vegge, T.; Honkala, K.; Hansen, H. A. Grand Canonical DFT Investigation of the CO2RR and HER Reaction Mechanisms on MoTe2 Edges. *J. Phys. Chem. C* **2023**, *127*, 18855−18864.

(69) Tang, W.; Sanville, E.; Henkelman, G. A grid-based Bader analysis algorithm without lattice bias. *J. Phys.: Condens. Matter* **2009**, *21*, No. 084204.

(70) Wang, H.; Fu, W.; Yang, X.; Huang, Z.; Li, J.; Zhang, H.; Wang, Y. Recent advancements in heterostructured interface engineering for hydrogen evolution reaction electrocatalysis. *Journal of Materials Chemistry A* **2020**, *8*, 6926−6956.

(71) Zhou, Y.; Wu, D.; Zhu, Y.; Cho, Y.; He, Q.; Yang, X.; Herrera, K.; Chu, Z.; Han, Y.; Downer, M. C.; Peng, H.; Lai, K. Out-of-Plane Piezoelectricity and Ferroelectricity in Layered α-In2Se3 Nanoflakes. *Nano Lett.* **2017**, *17*, 5508−5513.

(72) Tang, X.; Shang, J.; Ma, Y.; Gu, Y.; Chen, C.; Kou, L. Tuning Magnetism of Metal Porphyrazine Molecules by a Ferroelectric In2Se3Monolayer. *ACS Appl. Mater. Interfaces* **2020**, *12*, 39561−39566.

(73) Akhound, M.; Soleimani, M.; Pourfath, M. Controllable gas adsorption via inter-coupled ferroelectricity in In2Se3 monolayer. *Materials Today Chemistry* **2023**, *31*, No. 101626.

(74) Tang, X.; Shang, J.; Gu, Y.; Du, A.; Kou, L. Reversible gas capture using a ferroelectric switch and 2D molecule multiferroics on the In2Se3 monolayer. *Journal of Materials Chemistry A* **2020**, *8*, 7331−7338.

(75) Soleimani, M.; Pourfath, M. Ferroelectricity and phase transitions in In2Se3 van der Waals material. *Nanoscale* **2020**, *12*, 22688−22697.

(76) Wu, Q.; Huang, B.; Dai, Y.; Heine, T.; Ma, Y. Main-group metal elements as promising active centers for single-atom catalyst toward nitric oxide reduction reaction. *npj 2D Mater. Appl.* **2022**, *6*, 52.

(77) Greeley, J.; Nørskov, J. K. Electrochemical dissolution of surface alloys in acids: Thermodynamic trends from first-principles calculations. *Electrochim. Acta* **2007**, *52*, 5829−5836.

(78) Li, W.; Liu, C.; Gu, C.; Choi, J.-H.; Wang, S.; Jiang, J. Interlayer charge transfer regulates single-atom catalytic activity on electride/graphene 2D heterojunctions. *J. Am. Chem. Soc.* **2023**, *145*, 4774−4783.

(79) Maintz, S.; Deringer, V. L.; Tchougréeff, A. L.; Dronskowski, R. LOBSTER: A tool to extract chemical bonding from plane-wave based DFT. *J. Comput. Chem.* **2016**, *37*, 1030−1035.

(80) Li, Q.; Qiu, S.; Yan, M.; Liu, C.; Zhou, F.; Jia, B.; He, L.; Zhang, X.; Sun, C. Insight into the Reactivity of Carbon Structures for Nitrogen Reduction Reaction. *Langmuir* **2021**, *37*, 14657−14667.

(81) Chatt, J.; Dilworth, J. R.; Richards, R. L. Recent advances in the chemistry of nitrogen fixation. *Chem. Rev.* **1978**, *78*, 589−625.

(82) Seefeldt, L. C.; Hoffman, B. M.; Dean, D. R. Mechanism of Mo-Dependent Nitrogenase. *Annu. Rev. Biochem.* **2009**, *78*, 701−722.

(83) Hinnemann, B.; Nørskov, J. K. Catalysis by Enzymes: The Biological Ammonia Synthesis. *Top. Catal.* **2006**, *37*, 55−70.

(84) Anderson, J. S.; Rittle, J.; Peters, J. C. Catalytic conversion of nitrogen to ammonia by an iron model complex. *Nature* **2013**, *501*, 84−87.

(85) Hill, P. J.; Doyle, L. R.; Crawford, A. D.; Myers, W. K.; Ashley, A. E. Selective Catalytic Reduction of N2 to N2H4 by a Simple Fe Complex. *J. Am. Chem. Soc.* **2016**, *138*, 13521−13524.

(86) Bazhenova, T.; Shilov, A. Nitrogen fixation in solution. *Coord. Chem. Rev.* **1995**, *144*, 69−145.

(87) Huang, X.; Wang, J.; Zhao, C.; Gan, L.-Y.; Xu, H. NiO Matrix Decorated by Ru Single Atoms: Electron-Rich Ru-Induced High Activity and Selectivity toward Electrochemical N2 Reduction. *J. Phys. Chem. Lett.* **2023**, *14*, 3785−3793.

(88) Wan, S.; Li, Y.; Li, W.; Mao, X.; Zhu, W.; Zeng, H. Room-temperature ferroelectricity and a switchable diode effect in two-dimensional α-In2Se3 thin layers. *Nanoscale* **2018**, *10*, 14885−14892.

(89) Ma, B.; Peng, Y.; Ma, D.; Deng, Z.; Lu, Z. Boron-doped InSe monolayer as a promising electrocatalyst for nitrogen reduction into ammonia at ambient conditions. *Appl. Surf. Sci.* **2019**, *495*, 143463.

(90) Zhang, Y.; Wang, X.; Liu, T.; Dang, Q.; Zhu, L.; Luo, Y.; Jiang, J.; Tang, S. Charge and spin communication between dual metal single-atom sites on C 2 N sheets: regulating electronic spin moments of Fe atoms for N 2 activation and reduction. *Journal of Materials Chemistry A* **2022**, *10*, 23704−23711.

(91) Liu, X.; Jiao, Y.; Zheng, Y.; Jaroniec, M.; Qiao, S.-Z. Building up a picture of the electrocatalytic nitrogen reduction activity of transition metal single-atom catalysts. *J. Am. Chem. Soc.* **2019**, *141*, 9664−9672.

(92) Wu, T.; Fan, X.; Wang, C.; Wu, L.; Bai, Y.; Jia, G. The first principles study of the dual-atom catalyst based on g-C3N5 for efficient nitrogen fixation. *Appl. Surf. Sci.* **2025**, *682*, No. 161648.

(93) Pandiyan, K.; Dhanthala Chittibabu, D. K.; Chen, H.-T. Theoretical Establishment and Screening of Double-Atom Catalysts Supported on Biphenylene for an Efficient Electrocatalytic Nitrogen Reduction Reaction. *ACS Applied Energy Materials* **2024**, *7*, 10758−10769.